Hybrid Three-Level Full-Bridge Isolated Buck–Boost Converter With Clamped Inductor for Wider Voltage Range Application

Yan Li, *Member, IEEE*, Fang Li, Fang-Wei Zhao, *Student Member, IEEE*, Xiao-Jie You, Kun Zhang, and Mei Liang, *Member, IEEE*

***Abstract*—An isolated buck–boost (IBB) converter with a hybrid three-level full-bridge primary-side circuit is proposed to achieve wider voltage range regulation. The primary-side circuit is composed of a three-level leg and a two-level leg. The output voltage of the primary-side circuit is five level (i.e., $\pm V_{in}$, $\pm V_{in}/2$, and zero), and the secondary-side circuit is a semiactive full-bridge rectifier with two active switches and two diodes. The input voltage of the secondary-side circuit is three level (i.e., $\pm V_o$ and zero). Hence, the operation voltage range can be wider than the normal IBB converter's with three voltage levels in the primary-side circuit and secondary-side circuit. This paper focuses on the control strategy allowing the converter to operate in boundary current mode at heavy load and in discontinuous current mode at light load with smooth mode transition. The soft-switching performance and output characteristics of the proposed converter are presented in detail. Compared with the semi-dual active bridge converter, the voltage range is doubled and the peak current of the clamped inductor is decreased. An 800-W prototype with 100–400-V input voltage and 380-V output voltage is built and tested to verify the feasibility of the proposed control strategy.**

***Index Terms*—Boundary current mode (BCM), clamped inductor, discontinuous current mode (DCM), hybrid three level, isolated buck–boost (IBB) converter, wide voltage range.**

I. Introduction

THE ISOLATED converter with wide operation range and high conversion efficiency is needed in various applications, such as power supplies for servers, front-end converters, and power converters for solar array, fuel-cell, battery, or supercapacitor. There are three applications of wide voltage range converter; the first is constant input and variable output, the second is variable input and constant output,

Manuscript received January 12, 2018; revised April 26, 2018; accepted May 22, 2018. Date of publication June 6, 2019; date of current version February 5, 2019. This work was supported by the Lite-ON Power Electronics Technology Research Fund under Grant 2017-01. Recommended for publication by Associate Editor R.-L. Lin. *(Corresponding author: Yan Li.)*

Y. Li, F. Li, F.-W. Zhao, and X.-J. You are with the Institute of Power Electronics, Beijing Jiaotong University, Beijing 100044, China (e-mail:

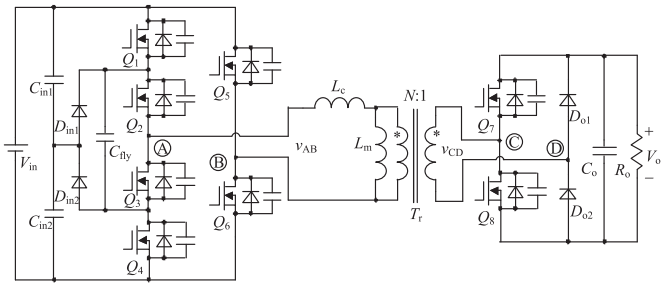

Fig. 1. Proposed hybrid three-level full-bridge IBB converter with clamped inductor.

The other types of wide voltage range converter are composed of different voltage levels at different operation modes. The special example is an *LLC* converter with semiactive variable-structure rectifier [3]. The output range of this converter is doubled by adaptively operating the secondary-side circuit as a voltage doubler ($\pm V_o/2$ and zero level in secondary-side port) or a voltage quadrupler ($\pm V_o/4$ and zero level in secondary-side port). In [13], the output voltage of variable-structure primary-side circuit can be $\pm V_{in}$ or $\pm V_{in}/2$ at different time. Moreover, the hybrid full-bridge three-level *LLC* resonant converter can operate in three-level mode and two-level mode with reduced input current ripple and output filter [14]. However, there are mode transitions between the two modes of these variable-structure converters.

Apart from above, an isolated buck–boost (IBB) converter is a family of converters comprised by primary-side circuit, ac link, and secondary-side circuit. There are active switches in both primary-side and secondary-side of IBB converter. Therefore, it can operate in buck or boost modes and regulate the input voltage in a wide range with high efficiency [15]–[18]. Dual active bridge (DAB) converter is an example of IBB converter in bidirectional applications [19], [20], and R is almost 1.5–2 in the experimental verifications in references. In paper [21], a dual-phase-shift control strategy of unidirectional semi-DAB converter is proposed, and the output current at different voltage gains and the peak current of the clamped inductor are analyzed. However, the current increasing and efficiency decline at maximum or minimum values of wide voltage range limit the application. In order to achieve wider voltage operation range (such as $R \geq 3$), high conversion efficiency, and smooth transition between different operating modes, a hybrid three-level full-bridge IBB converter and its control strategy will be proposed in this paper. With five variable voltage levels in primary-side port, i.e., $\pm V_{in}$, $\pm V_{in}/2$, and zero level, the converter can operate at a wider voltage range than normal IBB converters. Furthermore, voltage regulation with smooth mode transition under simple constant-frequency phase-shift control is another important issue in this paper.

This paper is organized as follows. Circuit topology and operational modes are analyzed in Section II, and an optimal control strategy is proposed in Section III. The output current and peak current are analyzed and compared, and the design considerations are presented in Section IV. In Section V, a simple and straightforward feedback controller is designed, and the experimental results are given. Finally, a summary and conclusions are presented in Section VI.

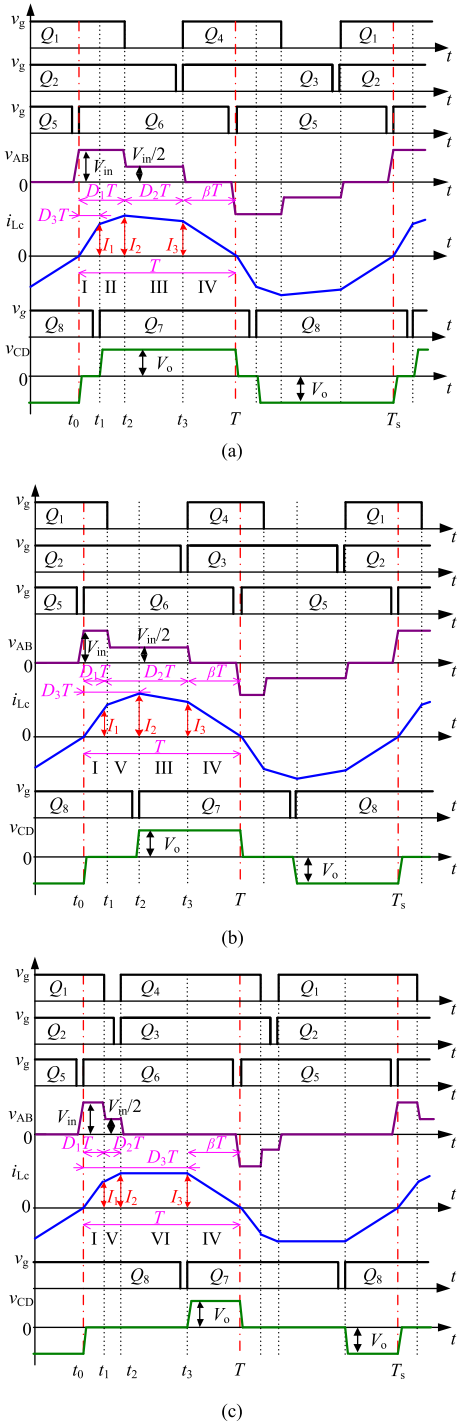

Fig. 2. Switching waveforms of the IBB converter in BCM mode at $0.5 < M < 1$. (a) $0 \leq D_3 < D_1$. (b) $D_1 \leq D_3 < D_1 + D_2$. (c) $D_3 \geq D_1 + D_2$.

II. Operational Principles

A. Topology Description

The proposed hybrid three-level full-bridge IBB converter with clamped inductor L_C is shown in Fig. 1. The primary-side

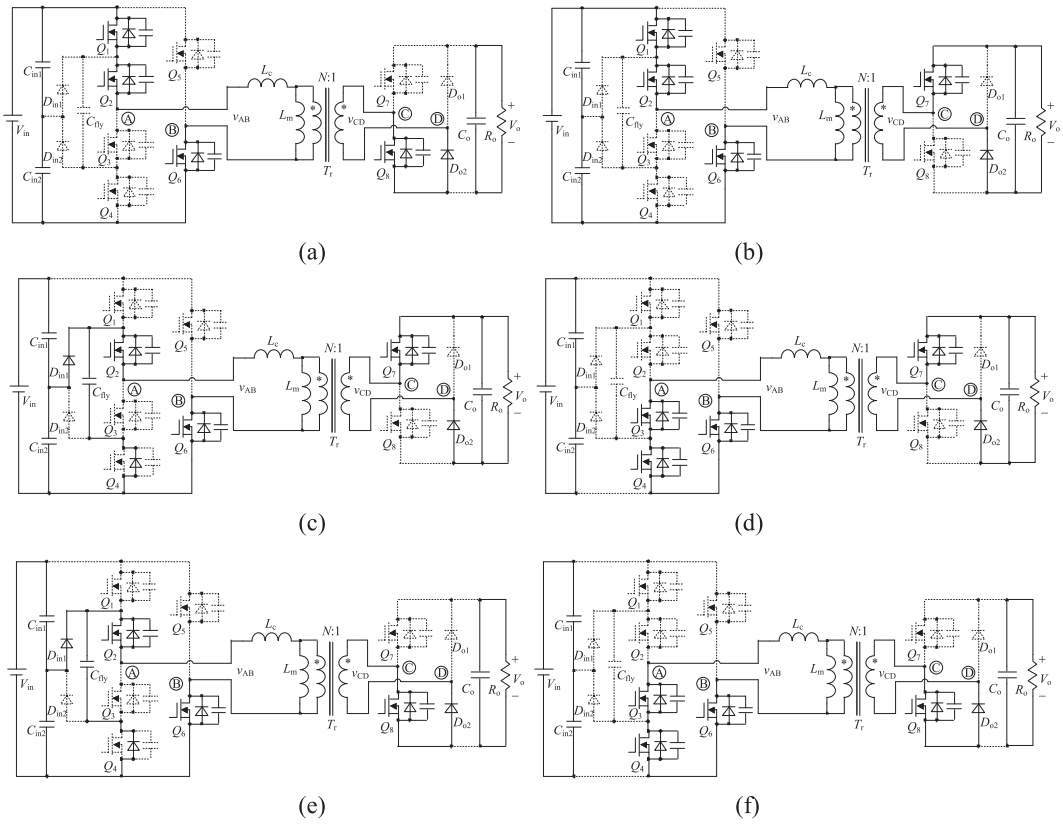

Fig. 3. Equivalent circuits for each operational state in positive half cycle. (a) State I. (b) State II. (c) State III. (d) State IV. (e) State V. (f) State VI.

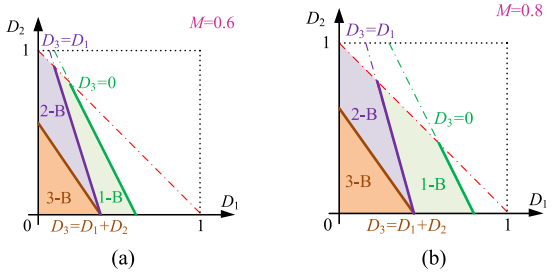

Fig. 4. Divisions of three operating areas at $0.5 < M < 1$ in BCM mode. (a) $M = 0.6$. (b) $M = 0.8$.

circuit is hybrid three-level full-bridge, and its output port is an AB port. The voltage levels of AB port could be $\pm V_{\text{in}}$, $\pm V_{\text{in}}/2$, and zero level. T_{s} is the switching period, set the start time t_0 as the time when the primary-side switches turn ON and v_{AB} changes from zero to positive level. The ending of positive half cycle T is the time v_{AB} changes from zero to negative level. $T_{\text{s}} = 2T$, and the equal switching frequency is f_{s}. We define D_1T as the length of time interval $v_{\text{AB}} = V_{\text{in}}$, D_2T as the length of time interval $v_{\text{AB}} = V_{\text{in}}/2$, $D_1 + D_2 \leq 1$. In the rest time, v_{AB} is the zero voltage.

The secondary-side circuit is a semiactive full-bridge rectifier with two active switches and two diodes, and its input port is a CD port. The voltage levels of CD port could be $\pm V_{\text{o}}$ and zero level. D_3T is defined as the length of time interval $v_{\text{CD}} = 0$ in positive half period. The current of L_{C} is clamped by the voltage across it, i.e., the difference between v_{AB} and v_{CD}. That is the reason why the inductor is named as clamped inductor.

To simplify the analysis, we suppose that $N = 1$. When $V_{\text{o}} = V_{\text{in}}$, $M = 1$ and when $V_{\text{o}} = V_{\text{in}}/2$, $M = 0.5$. Therefore, M can be divided into three intervals: $M \leq 0.5$, $0.5 < M < 1$, and $M \geq 1$. The duty cycle of all the switches are fixed at 0.5, and the converter is under simple fixed-frequency phase-shift control with three control variables: D_1, D_2, and D_3.

If the voltage leads the current of AB port, the converter is in CCM mode with backflow power. The ZVS ON of primary-side switches can be achieved. However, the RMS current value and peak current value are larger, leading to increasing of conduction loss and the current stress of devices. That is one of the reasons why the operational mode of the proposed converter is limited in boundary current mode (BCM) or discontinuous current mode (DCM) mode. There is no backflow power, and zero current switching (ZCS) of some devices can be achieved. The other reason is that the control variables could be simplified. In this paper, we use D_1 and D_2 as active control variables, D_3 as the indirect variable that can be calculate from D_1, D_2, and the operational mode. This simplification has great significance for the research of this paper.

B. Operational Modes

1) BCM Mode When 0.5 < M < 1: Fig. 2 shows the operational waveforms of the IBB converter in BCM mode when $0.5 < M < 1$. Three subwaveforms are $0 \leq D_3 < D_1$,

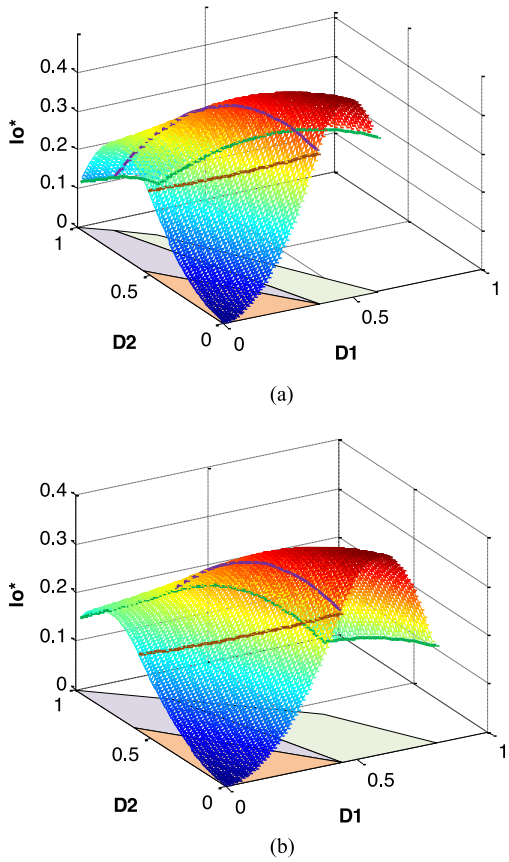

Fig. 5. Three-dimensional graphs of I_o^* versus D_1, D_2 at $0.5 < M < 1$ in BCM mode. (a) $M = 0.6$. (b) $M = 0.8$.

$D_1 \le D_3 < D_1 + D_2$, $D_3 \ge D_1 + D_2$, respectively, and named as 1-B mode, 2-B mode, and 3-B mode. Due to the symmetry of the circuit, only six states in positive half cycle are analyzed here and corresponding equivalent circuits are shown in Fig. 3, without consideration the effect of dead time.

State I [t_0, t_1] of Fig. 2(a)*:* In CCM mode, the current of a clamped inductor is zero at t_0. The voltage across the clamped inductor in state I is V_{in}, and the current increases linearly until the end of D_3T. The current of a clamped inductor satisfies

$$I_1 = i_{Lc}(t_1) = i_{Lc}(t_0) + \frac{V_{\text{in}} D_3 T}{L_c} = \frac{V_{\text{in}} D_3 T}{L_c}. \quad (1)$$

State II [t_1, t_2] of Fig. 2(a)*:* At t_1, Q_7 turns OFF and Q_8 turns ON, the voltage across the clamped inductor is V_{in}–V_{o}. When $0.5 < M < 1$, V_{in} is larger than V_{o}, and the current of a clamped inductor increases with a new slope. The length of state II is D_1T–D_3T, and

$$I_2 = I_1 + \frac{(V_{\text{in}} - V_{\text{o}})(D_1 - D_3)T}{L_c}. \quad (2)$$

State III [t_2, t_3] of Fig. 2(a)*:* At t_2, Q_1 turns OFF and Q_4 turns ON, the voltage across the clamped inductor is V_{in}/ 2- V_{o}. When $0.5 < M < 1$, V_{in}/ 2 is less than V_{o}, and the current of a clamped inductor decreases at this state. The length of state III is D_2T,

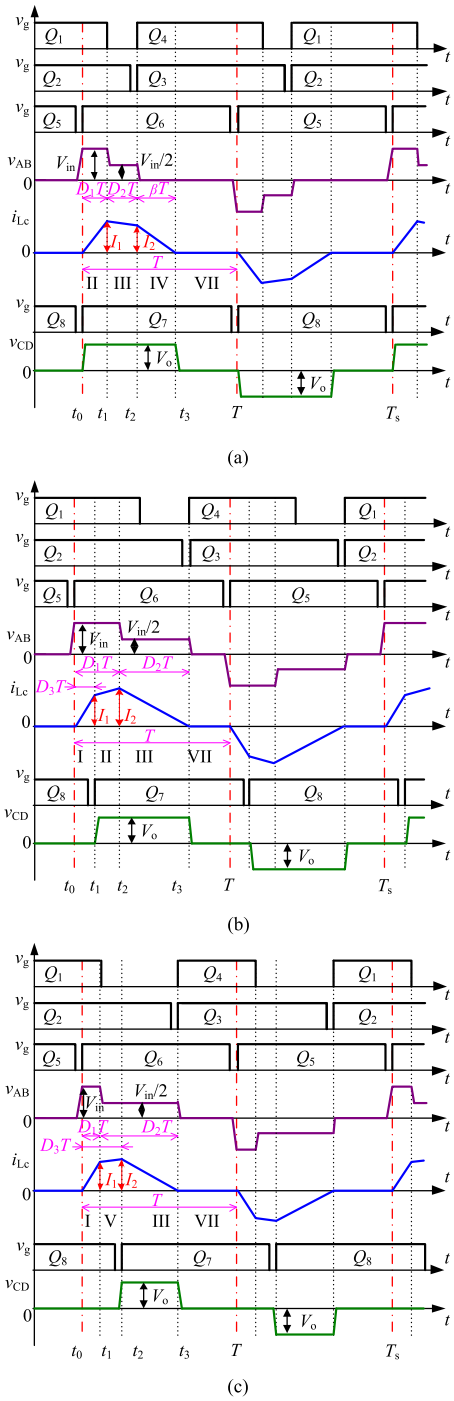

Fig. 6. Switching waveforms of the IBB converter in DCM mode at $0.5 < M < 1$. (a) $D_3 = 0$. (b) $0 < D_3 < D_1$. (c) $D_1 \le D_3 < D_1 + D_2$.

and

$$I_3 = I_2 + \left(\frac{V_{\text{in}}}{2} - V_o\right)\frac{D_2 T}{L_c}. \quad (3)$$

State IV [t_3, T] of Fig. 2(a)*:* At t_3, Q_2 turns OFF and Q_3 turns ON, the voltage across the clamped inductor is $-V_{\text{o}}$. The current of a clamped inductor decreases. Assume the length of

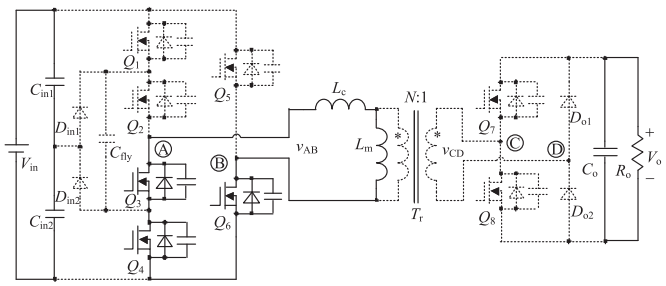

Fig. 7. Equivalent circuit of state VII.

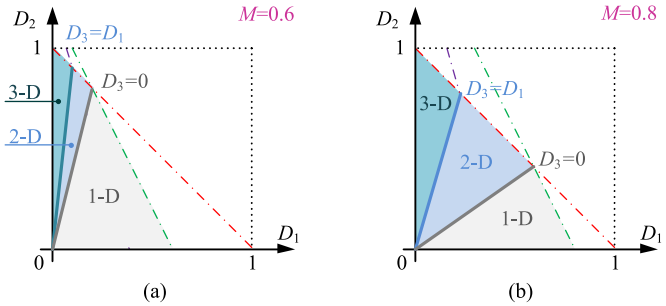

Fig. 8. Divisions of three operating areas at $0.5 < M < 1$ in DCM mode. (a) $M = 0.6$. (b) $M = 0.8$.

the interval that the current decreases from I_3 to zero is βT, and

$$\beta T = \frac{I_3 L_c}{V_o}. \tag{4}$$

State V [t_1, t_2] of Fig. 2(b)*:* If $D_1 \le D_3 < D_1 + D_2$, state V follows state I. The voltage across the clamped inductor is $V_{in}/2$. The current of a clamped inductor increases at half slope of state I, and the currents in Fig. 2(b) are

$$\begin{cases} I_1 = \frac{V_{in} D_1 T}{L_c} \\ I_2 = I_1 + \frac{V_{in}}{2} \frac{(D_3 - D_1)T}{L_c} \\ I_3 = I_2 + \left(\frac{V_{in}}{2} - V_o\right) \frac{(D_1 + D_2 - D_3)T}{L_c}. \end{cases} \tag{5}$$

After state V, next comes state III and state IV, and βT in Fig. 2(b) also satisfies (4).

State VI [t_2, t_3] of Fig. 2(c)*:* If $D_3 \ge D_1 + D_2$, state VI follows state I and state V. The voltage across the clamped inductor is zero, and the current maintains the same at state VI in ideal case

$$I_3 = I_2 = I_1 + \frac{V_{in}}{2} \frac{D_2 T}{L_c} = \frac{V_{in} D_1 T}{L_c} + \frac{V_{in}}{2} \frac{D_2 T}{L_c}. \tag{6}$$

After state VI, next comes state IV, and βT in Fig. 2(c) also satisfies (4).

In BCM mode, the current of a clamped inductor increases from zero at the beginning of each half period, and decreases to zero at the ending of each half period. The condition $D_1 + D_2 + \beta = 1$ requires to be satisfied in BCM mode. The simplification is

$$D_3 = 1 - \frac{D_1 + \frac{D_2}{2}}{M}. \tag{7}$$

The boundary between the three operating areas is determined by $D_3 = 0$, $D_3 = D_1$, $D_3 = D_1 + D_2$, and can be solved as follows:

$$\begin{cases} D_3 = 0 : D_1 + \frac{D_2}{2} = M \\ D_3 = D_1 : D_1 (1 + M) + \frac{D_2}{2} = M \\ D_3 = D_1 + D_2 : D_1 (1 + M) + D_2 \left(M + \frac{1}{2}\right) = M. \end{cases} \tag{8}$$

The conditions $D_1 \ge 0$, $D_2 \ge 0$, and $D_1 + D_2 \le 1$ should be satisfied at the same time. Set D_1 as the variable of horizontal coordinate, D_2 as the variable of vertical coordinate, and then we draw the different boundary conditions of $M = 0.6$ and $M = 0.8$ in Fig. 4.

The output currents of three operating areas are (9) shown at the bottom of this page.

Usually, the current quantities are normalized to the base $I_{base} = V/\omega L$. In this paper, we use $I_{\_base} = V_o T/2L_c$ to normalize the output current, and draw the 3-D graphs of I_o^* versus D_1, D_2 at $0.5 < M < 1$ in BCM mode in Fig. 5.

2) DCM Mode When 0.5 < M < 1: However, when the load is light, it is not suitable to operate in BCM mode, but DCM mode. The operational waveforms in DCM mode are shown in Fig. 6. Three subwaveforms are $D_3 = 0$, $0 < D_3 \le D_1$, and $D_3 > D_1$, respectively, and named as 1-D mode, 2-D mode, and 3-D mode. In 2-D mode and 3-D mode, $\beta = 0$ that means the current of a clamped inductor decreases to zero at the end of state III. As a result, the control variables are simplified.

There is one more state in DCM mode than BCM mode. The equivalent circuit of state VII is shown in Fig. 7. Similar to state VI, the voltage across the clamped inductor in state VII is zero. The difference is the current maintains zero in state VII in ideal case.

In Fig. 6(a), the current of a clamped inductor and time length βT satisfy

$$\begin{cases} I_1 = \frac{(V_{in} - V_o) D_1 T}{L_c} \\ I_2 = I_1 + \frac{(V_{in}/2 - V_o) D_2 T}{L_c} \\ \beta T = \frac{I_2 L_c}{V_o}. \end{cases} \tag{10}$$

$$\begin{cases} 1 - B : I_o = \frac{V_o T}{2L_c} \left(-\frac{(2D_1 + D_2)^2}{4M^3} - \frac{(1+M)\left({D_1}^2 + D_1 D_2 - 2D_1 + \frac{{D_2}^2}{4} - D_2\right)}{M^2} - \frac{\frac{{D_2}^2}{4} + 1}{M} \right) \\ 2 - B : I_o = \frac{V_o T}{2L_c} \left(-\frac{(2D_1 + D_2)^2}{8M^3} - \frac{(2D_1 + D_2)(D_2 - 2)}{4M^2} - \frac{(D_1 + D_2 - 1)^2}{2M} \right) \\ 3 - B : I_o = \frac{V_o T}{2L_c} \frac{\left(D_1 + \frac{D_2}{2}\right)^2}{M^2}. \end{cases} \tag{9}$$

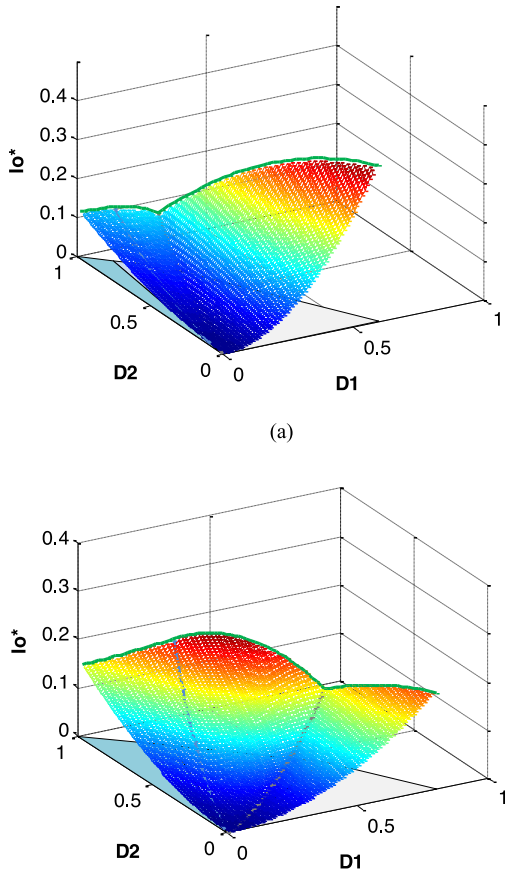

Fig. 9. Three-dimensional graphs of I_o^* versus D_1, D_2 at $0.5 < M < 1$ in DCM mode. (a) $M = 0.6$. (b) $M = 0.8$.

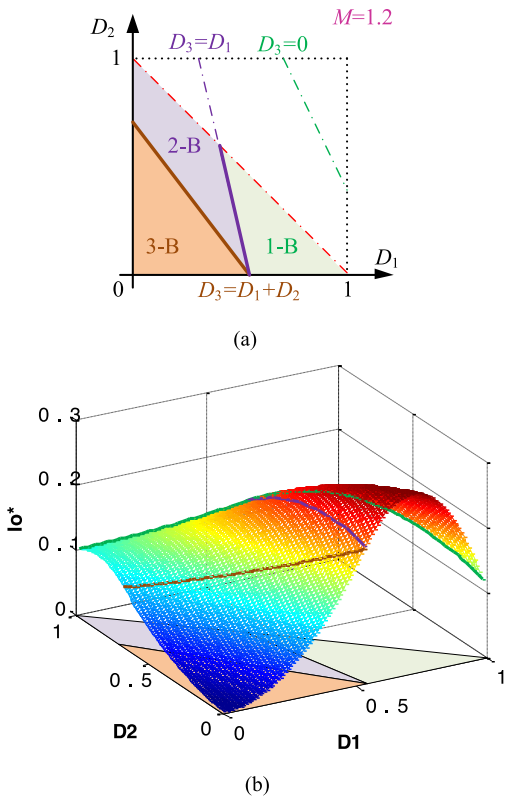

Fig. 10. Graphs at $M = 1.2$ in BCM mode. (a) Divisions of three operational areas. (b) Three-dimensional graphs of I_o^* versus D_1, D_2.

Based on the condition of DCM mode, β can be derived as

$$\beta = \frac{D_1\,(1-M) + D_2\,(0.5-M)}{M}. \tag{11}$$

In addition, βT need to satisfy $D_1 + D_2 + \beta \le 1$, hence

$$D_1 + \frac{D_2}{2} \le M \tag{12}$$

which is similar to the condition $D_3 = 0$ in 1-B mode.

In Fig. 6(b), the first three states of mode 2-D are the same with the first three states of mode 1-B. 2-D mode need to satisfy $0 < D_3 < D_1$ and $\beta = 0$. D_3 can be derived as

$$D_3 = \frac{D_1\,(M-1) + D_2\,(M-0.5)}{M}. \tag{13}$$

The boundary condition between 1-D mode and 2-D mode is $D_3 = 0$, hence

$$\frac{D_2}{D_1} = \frac{2-2M}{2M-1}. \tag{14}$$

In Fig. 6(c), the first three states of mode 3-D are the same with the first three states of mode 2-B. 3-D mode need to satisfy $D_1 \le D_3 < D_1 + D_2$ and $\beta = 0$. D_3 can be derived as (13). The boundary condition between 2-D mode and 3-D mode is $D_3 = 0$, hence

$$\frac{D_2}{D_1} = \frac{2}{2M-1}. \tag{15}$$

Above all, the different boundary conditions of $M = 0.6$ and $M = 0.8$ in DCM mode are shown in Fig. 8. The dotted lines are the boundaries in BCM mode. We can see the boundaries of DCM mode and BCM mode across at two points on the line $D_1 + D_2 = 1$. The conclusion also can be obtained by mathematical calculation.

The output currents of three operating areas are

$$\begin{cases} 1\text{–D}: I_o = \frac{V_o T}{2L_c}\frac{\left({D_1}^2 - M{D_1}^2 + D_1 D_2 - M D_1 D_2 + \frac{{D_2}^2}{4} - \frac{M{D_2}^2}{2}\right)}{M^2} \\ 2-\text{D}: I_o = \frac{V_o T}{2L_c}\left(-\frac{(2D_1+D_2)^2}{4M^3} + \frac{{D_1}^2 + 2D_1 D_2 + \frac{3{D_2}^2}{4}}{M^2} - \frac{{D_2}^2}{2M}\right) \\ 3-\text{D}: I_o = \frac{V_o T}{2L_c}\frac{(2M-1)\left(D_1 + \frac{D_2}{2}\right)^2}{2M^3}. \end{cases} \tag{16}$$

We also use $I_{\text{base}} = V_o T / 2L_c$ to normalize the output current and draw the 3-D graphs of I_o^* versus D_1, D_2 at $0.5 < M < 1$ in DCM mode in Fig. 9.

The graphs in Figs. 5 and 9 both pass point (0, 0, 0), and cross at the line when $D_1 + D_2 = 1$ and $D_3 = 0$.

3) Other Modes: When $M \ge 1$ in BCM mode, $V_{\text{in}} \le V_o$. Therefore, the current of a clamped inductor decreases in state II of 1-B mode, and I_2 is not the peak value any more while I_1 is the peak value. The mathematical calculation results of $M \ge$

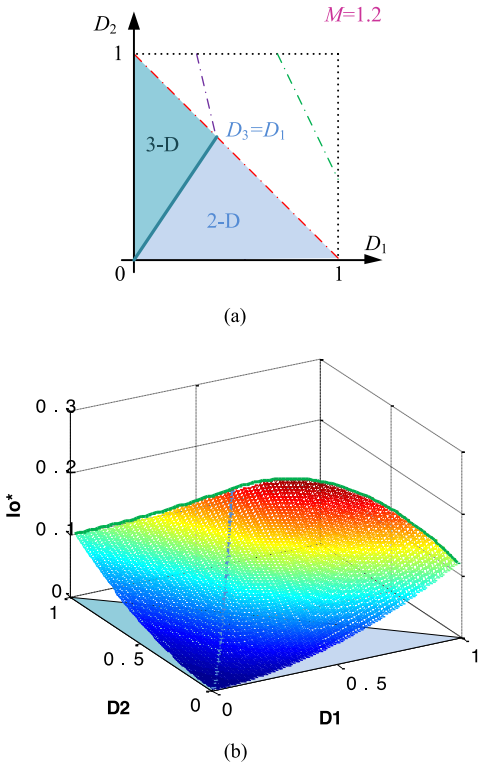

Fig. 11. Graphs at $M = 1.2$ in DCM mode. (a) Divisions of three operational areas. (b) Three-dimensional graphs of I_o^* versus D_1, D_2.

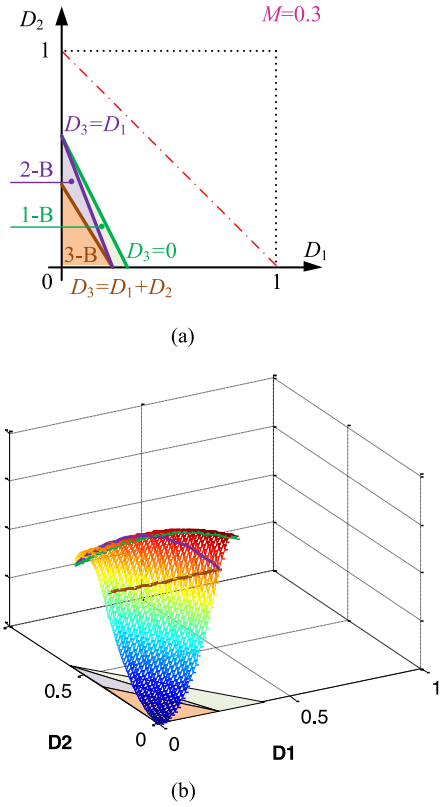

Fig. 12. Graphs at $M = 0.3$ in BCM mode. (a) Divisions of three operational areas. (b) Three-dimensional graphs of I_o^* versus D_1, D_2.

1 are the same to that when $0.5 < M < 1$. Line $D_3 = 0$ is not cross with $D_1 + D_2 = 1$. Divisions of three operational areas and 3-D graphs of I_o^* versus D_1, D_2 at $M = 1.2$ in BCM mode are shown in Fig. 10.

When $M \geq 1$ in DCM mode, only 2-D mode and 3-D mode exist. The boundary between 1-B mode and 2-B mode and the boundary between 2-D mode and 3-D mode are crossing at one point. Divisions of two operational areas and 3-D graphs of I_o^* versus D_1, D_2 at $M = 1.2$ in DCM mode are shown in Fig. 11.

When $M \leq 0.5$ in BCM mode, $V_{in}2 \geq V_o$. Therefore, the current of a clamped inductor increases in state III of 1-B mode and 1-B mode, and I_2 is not the peak value any more while I_3 is the peak value. $D_3 = 0$ is not across $D_1 + D_2 = 1$. Divisions of three operational areas and 3-D graphs of I_o^* versus D_1, D_2 at $M = 0.3$ in BCM mode are shown in Fig. 12.

When $M \leq 0.5$ in DCM mode, only 1-D mode exists, and I_2 is the peak value. Divisions of three operational areas and 3-D graphs of I_o^* versus D_1, D_2 at $M = 0.3$ in DCM mode are shown in Fig. 13.

III. Optimal Control Strategy

There is a maximum value of output current in 1-B mode, the values of variables and the current of this point are

$$D_{1\_max} = \frac{M^2 + M}{M^2 + M + 1}, D_{2\_max} = 0$$

$$D_{3\_max} = \frac{M^2}{M^2 + M + 1}, I_{o\_max} = \frac{1}{M^2 + M + 1}. \quad (17)$$

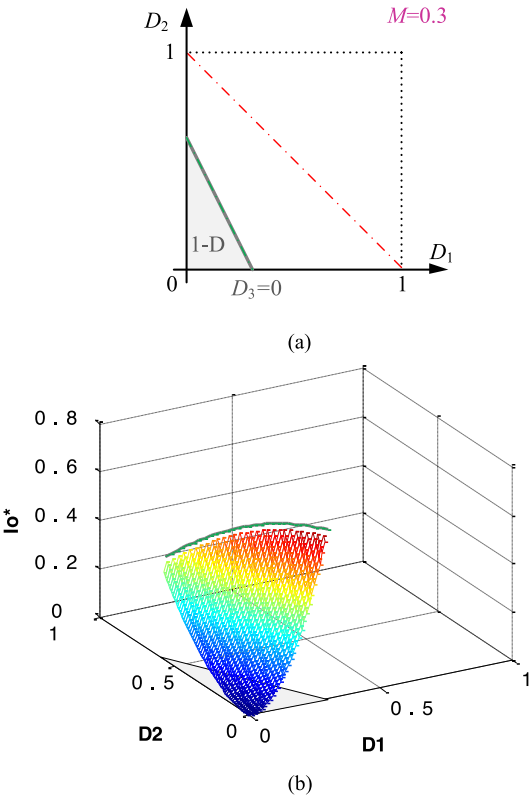

Fig. 13. Graphs at $M = 0.3$ in DCM mode. (a) Divisions of three operational areas. (b) Three-dimensional graphs of I_o^* versus D_1, D_2.

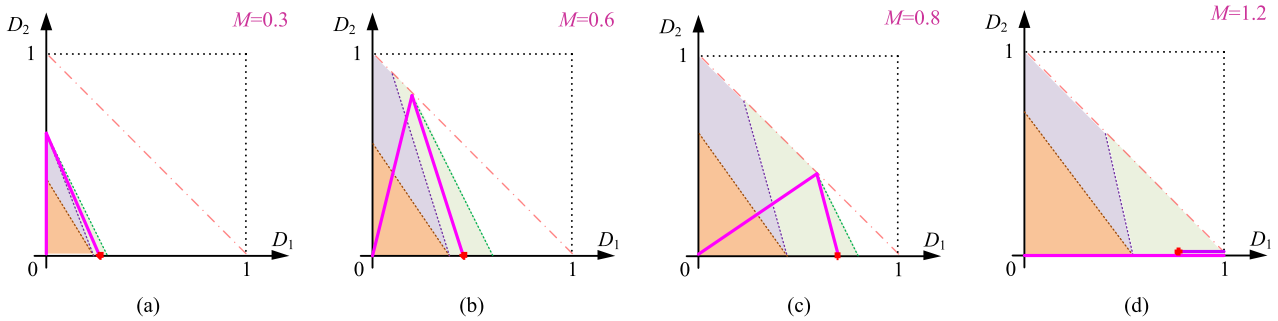

Fig. 14. Optimal control strategies in 3-D graphs. (a) $M = 0.3$. (b) $M = 0.6$. (c) $M = 0.8$. (d) $M = 1.2$.

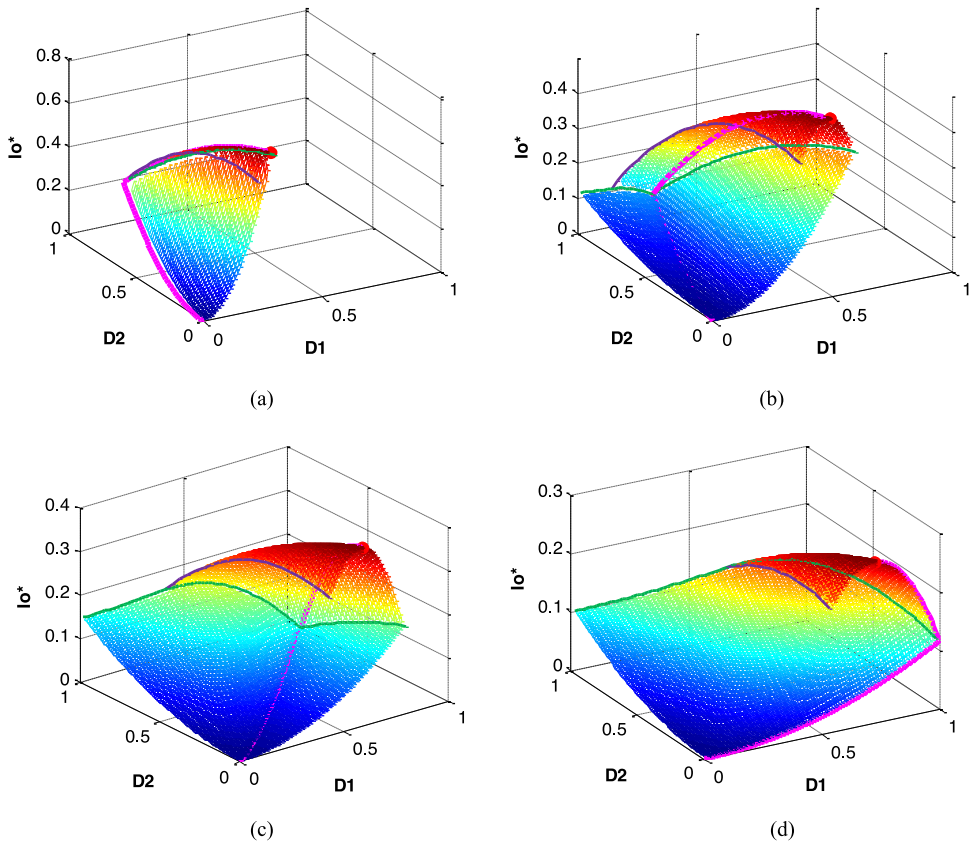

Fig. 15. Optimal control strategies in 3-D graphs. (a) $M = 0.3$. (b) $M = 0.6$. (c) $M = 0.8$. (d) $M = 1.2$.

The current of a clamped inductor reflects the current of transfer and power devices. The lower the peak current of the clamped inductor, the less RMS current and less conduction loss and switching loss of the converter will be. The optimal control strategy should be set at the operational point with the lowest peak current value, and can be listed as the optimization problem

$$\begin{aligned} &\min : \text{peak of } i_{Lc} \\ &\text{s.t.} \quad \text{same } I_o. \end{aligned} \tag{18}$$

where min means minimum, and s.t. means subject to.

A. Control Trajectories When $0.5 < M < 1$

The peak current values of the clamped inductor in BCM mode and DCM mode are

$$\begin{cases} 1-B: I_2 = \frac{V_o T}{2L_c} 2\left(1 - D_1 - \frac{D_2}{2M}\right) \\ 2-B: I_2 = \frac{V_o T}{2L_c}\left(\frac{2M + 2MD_1 - 2D_1 - D_2}{2M^2}\right) \\ 3-B: I_2 = \frac{V_o T}{2L_c}\frac{(2D_1 + D_2)}{M} \end{cases} \tag{19a}$$

$$\begin{cases} 1-D: I_1 = \frac{V_o T}{2L_c} 2\left(1 - M\right) D_1 \\ 2-D: I_2 = \frac{V_o T}{2L_c}\left(2M - 1\right) D_2 \\ 3-D: I_2 = \frac{V_o T}{2L_c}\frac{(2M-1)(2D_1 + D_2)}{2M^2}. \end{cases} \tag{19b}$$

TABLE I
SOFT-SWITCHING PERFORMANCE OF THE PROPOSED IBB CONVERTER WITH CLAMPED INDUCTOR

M	DCM	BCM
$M \leq 0.5$	Q_1、Q_4 OFF，Q_2、Q_3 ZVS ON； Q_5~Q_8 ZCS ON&OFF；	
$0.5<M<1$	Q_1、Q_4 ZCS ON； Q_2、Q_3、Q_5、Q_6 ZCS ON&OFF； Q_7~Q_8 ZCS ON&OFF；	Q_1~Q_4、Q_7、Q_8 ZVS ON； Q_5、Q_6 ZCS ON&OFF；
$M \geq 1$	Q_1~Q_6 ZCS ON&OFF； Q_7、Q_8 ZVS ON；	

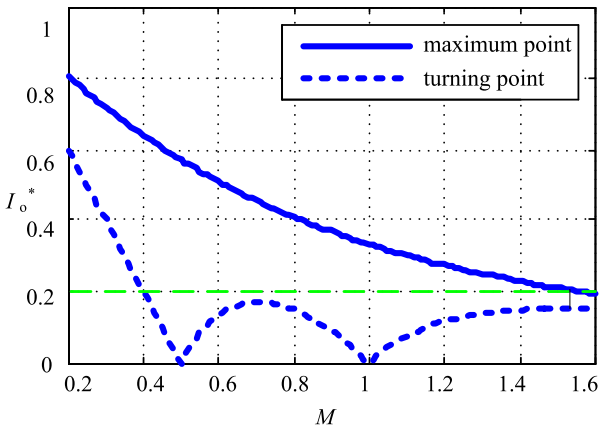

Fig. 16. Normalized output currents of maximum point and turning point at different M.

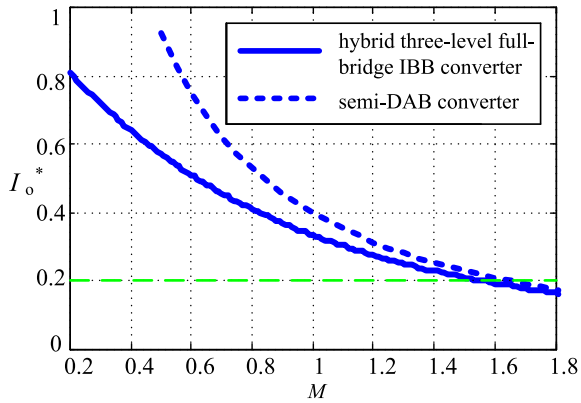

Fig. 17. Comparison of normalized maximum output currents at different M.

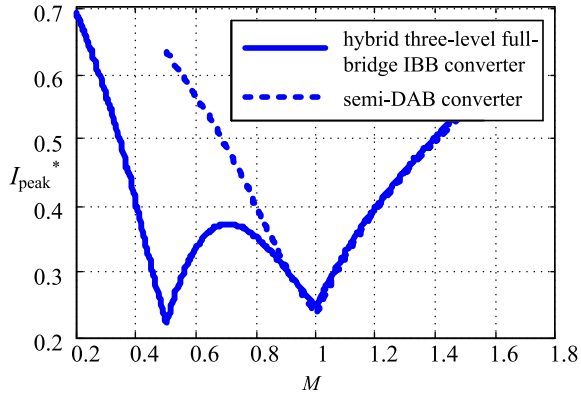

Fig. 18. Comparison of peak currents of clamped inductor with the same output current at different M.

Solve the optimal solution and the results are

$$\begin{cases} \text{DCM}: \frac{D_2}{D_1} = \frac{2-2M}{2M-1} \\ \text{BCM}: D_1\left(2-2M^3\right) + D_2\left(1-2M^3\right) = 2M - 2M^3 \end{cases}. \tag{20}$$

The optimal control trajectory is comprised of two stages. The first is in 1-D mode at light load, and the other is in 1-B mode at heavy load. In addition, there is a turning point between the two stages. In the first stage, $D_3 = 0$, D_1 and D_2 are increasing with the increase of the output power until $D_1 + D_2 = 1$. The turning point is $D_1 = 2M - 1$, $D_2 = 2 - 2M$. Then, the converter transits to the second stage, during which $D_3 > 0$, D_1, D_2, and D_3 are all varied to regulate the output power. During the two stages, the variables are changing continuously. The optimal control trajectories in 2-D and 3-D graphs and in *XOY* plane of $M = 0.6$ and $M = 0.8$ are shown in Figs. 14(b), (c) and 15(b), (c).

B. Control Strategy When $M \geq 1$ and $M \leq 0.5$

Using the same method, the optimal control trajectories when $M \geq 1$ are

$$\begin{cases} \text{DCM}: D_2 = 0 \\ \text{BCM}: D_2 = 0. \end{cases} \tag{21}$$

When $M > 1$, the first stage is in 2-D mode with $D_2 = 0$, D_1 and D_2 are changing with the increase of the output power until $D_1 = 1$. The turning point of the two stages is $D_1 = 1$, $D_2 = 0$. Then, the converter transits to the second stage, 1-B mode with $D_2 = 0$. D_1 is decreasing and D_3 is increasing until the maximum output point. That means $\pm V_{in}/2$ voltage levels no longer exist when $M > 1$. The optimal control trajectories when $M = 1.2$ are shown in Figs. 14(d) and 15(d).

Similarly, the optimal control trajectories when $M \leq 0.5$ can be solved and listed as

$$\begin{cases} \text{DCM}: D_1 = 0 \\ \text{BCM}: D_1\left(M^2 + M + 1\right) + D_2\frac{(1+M)}{2} = M^2 + M. \end{cases} \tag{22}$$

When $M < 0.5$, the input voltage is large. The first stage is in 1-D mode with $D_1 = 0$ and $D_3 = 0$, when only D_2 is increasing with the output power. The turning point between the two stages is $D_1 = 0$, $D_2 = 2M$. The converter transits to the second stage in 1-B mode. The ending of the second stage is also the maximum output point. The optimal control trajectories in 2-D and 3-D graphs and in *XOY* plane of $M = 0.3$ are shown in Figs. 14(a) and 15(a).

When $M = 0.5$, the turning point between the two stages of optimal control trajectories is $D_1 = 0$, $D_2 = 1$. When $M = 1$, the

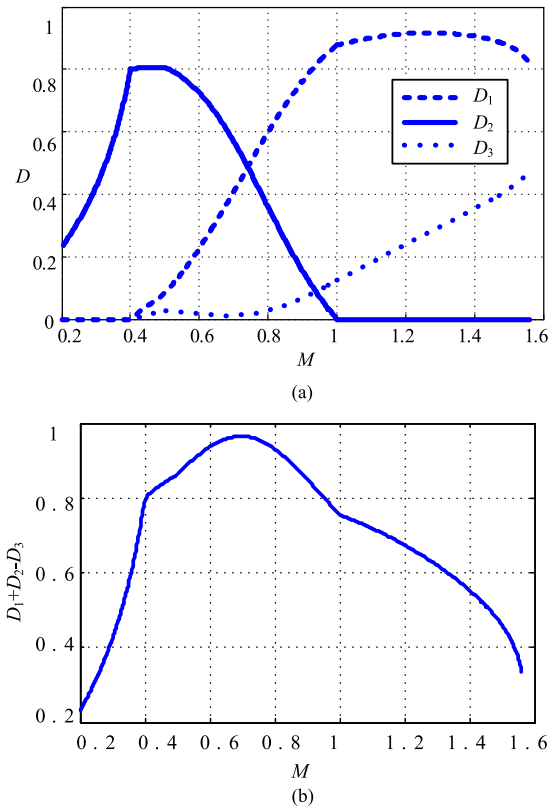

Fig. 19. Curves of duty ratio at different M when $I_o^* = 0.2$. (a) Duty ratios D_1, D_2, and D_3. (b) Duty ratio of direct energy transmission time.

turning point is $D_1 = 1$, $D_2 = 0$. As a result, the optimal control trajectories are changing continuously with the increasing of value of M. Therefore, the converter under this control strategy can regulate smoothly in the full output-power range and input–voltage range.

IV. Output Characteristics

A. Soft-Switching Performance

Due to the switches number and operational modes of hybrid three-level full-bridge IBB converter being large, Table I shows the soft-switching performance of BCM mode and DCM mode when M is different.

The current of a clamped inductor in dead zone contains magnetizing current of transformer and the equivalent load current. It is easy to realize ZVS of each switch in the converter. The switching loss of ZCS operation of MOSFET is far less than that with hard-switching operation. As a result, the converter has a potential to maintain high efficiency in a wide range.

B. Output Current

The output currents of turning points are

$$\begin{cases} M \le 0.5 : I_o = \frac{V_o T}{2L_c}(1-2M) \\ 0.5 < M < 1 : I_o = \frac{V_o T}{2L_c}\frac{\left(-2M^2+3M-1\right)}{M} \\ 1 \le M : I_o = \frac{V_o T}{2L_c}\frac{(M-1)}{M^3} \end{cases} \tag{23}$$

TABLE II
Parameters of the Proposed Converter

Components	Parameters
Input voltage	100~400V
Output voltage	380V
Maximum output power	800W
Switching frequency	60kHz
Turns ratio of transformer	14:38
Clamped inductor	19uH
Primary-side capacitors(C_{in1},C_{in2},C_{fly})	20uF
Primary-side MOSFETs(Q_1~Q_4)	IPB200N25N3GATMA
Primary-side MOSFETs(Q_5、Q_6)	IPB65R110CFD
Primary-side diodes(D_{in1}、D_{in2})	MBRB40250TG
Secondary-side MOSFETs(Q_7、Q_8)	IPB65R190C7
Secondary-side diodes(D_{o1}、D_{o2})	VS-16CDU06-M3/I

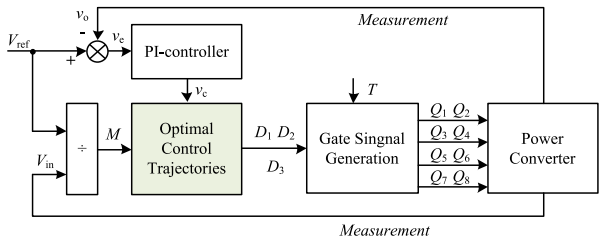

Fig. 20. Control block diagram of a hybrid three-level full-bridge IBB converter.

and these currents can be normalized by $I_{\_base=} V_o T/2L_c$. We draw the normalized output currents of turning points and maximum output point at different M values in Fig. 16. With constant switching frequency, the input voltage decreases as M increases, and the clamped inductor current becomes smaller, which means the maximum output current is reduced as well. Therefore, the output current should be reduced when the input voltage is very low. It can be found that when $M = 0.5$ and $M = 1$, the output power corresponding to the turning point is zero. The voltages of AB port and CD port are the same, $V_{in}/2 = V_o$ or $V_{in} = V_o$, and the voltage across the clamped inductor is zero. There is no power translating at the turning point.

Compared with the semi-DAB converter under dual-phase-shift control, the normalized maximum output current of a hybrid three-level full-bridge IBB converter under three variables control is decreasing lightly, as shown in Fig. 17. However, the constant load current is not affected all that much for it is limited by the maximum value of M.

C. Peak Current of the Clamped Inductor

Draw $I_o^* = 0.2$ to Fig. 18, it is a straight line which is paralleled to the horizontal axis. Solving the operational point and calculating the peak current of the clamped inductor, we can

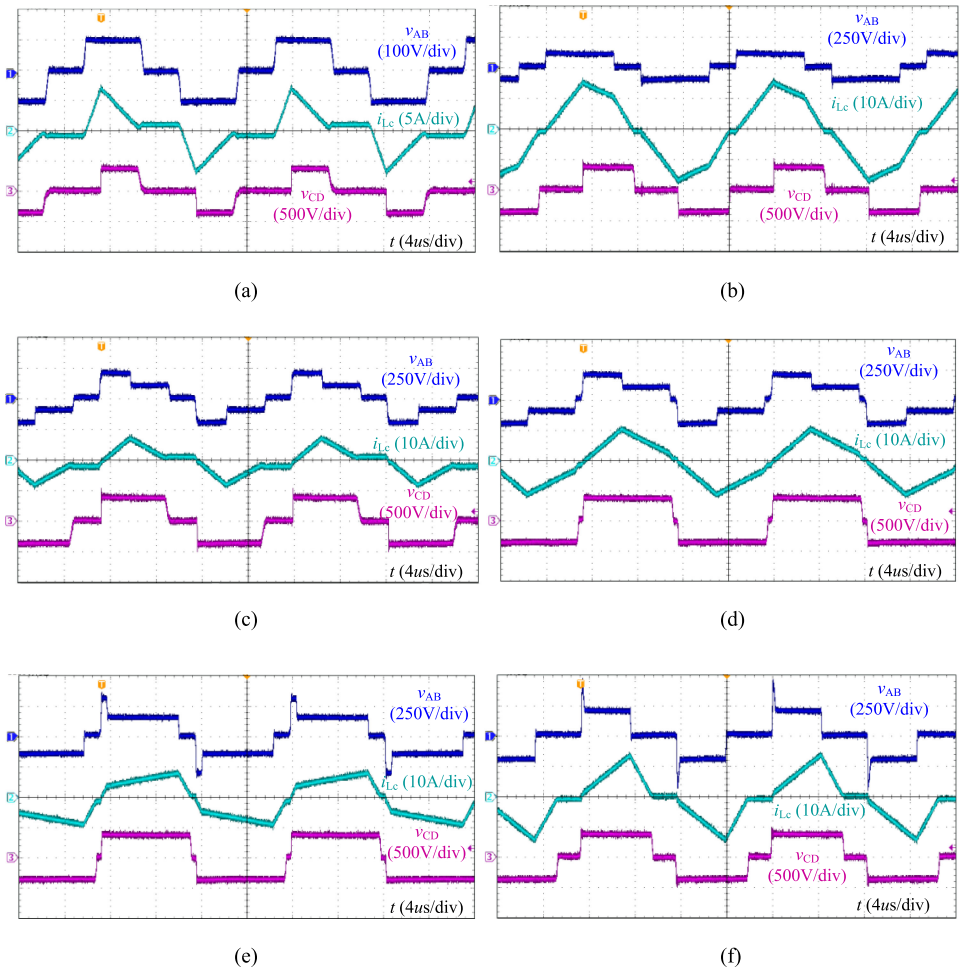

Fig. 21. Experimental waveforms at different operational areas. (a) $V_{in} = 100$ V, $P_o = 200$ W. (b) $V_{in} = 100$ V, $P_o = 800$ W. (c) $V_{in} = 200$ V, $P_o = 400$ W. (d) $V_{in} = 200$ V, $P_o = 800$ W. (e) $V_{in} = 300$ V, $P_o = 800$ W. (f) $V_{in} = 400$ V, $P_o = 800$ W.

draw the curve of a peak current of the clamped inductor at the same output current, as shown in Fig. 19. The peak current of the clamped inductor is the least at $M = 0.5$ and $M = 1$, when the voltages of AB port and CD port are approximate to each other. In addition, the peak current increases when M is far away from these two points. In the interval of $M \in [0.4, 1.2]$, the normalized peak current is less than 0.4, the twice of the output current. Compared with the semi-DAB converter under dual-phase-shift control, the peak current of the clamped inductor reduces obviously in the vicinity of $M = 0.5$ of hybrid three-level full-bridge IBB converter. Figs. 17–19 verify that the hybrid three-level full-bridge IBB converter under optimal control can operate in a wide voltage range.

D. Duty Ratio of Direct Energy Transmission Time

When $I_o^* = 0.2$, the duty ratios D_1, D_2, and D_3 are changed at different M, and the curves are shown in Fig. 19(a). Although the operation mode changes when the input voltage changes continuously at the constant load power, the duty ratios will change continuously without mutation. If the voltages of AB port are $\pm V_{in}$ or $\pm V_{in}/2$ and CD port is V_o, the energy transmit from the input port to the output port directly, and it is named as direct energy transmission. The bigger the direct energy transmission, the higher the efficiency of the converter will be. The duty ratio of direct energy transmission time is $D_1 + D_2 - D_3$, and its curve is shown in Fig. 19 (b). In the wider range of M, the duty ratio of direct energy transmission time is greater than 0.5. Fig. 19 shows that the hybrid three-level full-bridge IBB converter can regulate continuously and smoothly and have the potential to achieve high efficiency at a wide range of M.

From all above, there is a tradeoff between I_o^* and M of the parameter design considerations. If I_o^* is too large, the range of M is declined. Otherwise, if M is too wide, the peak current will increase significantly. In this paper, we choose $M_{min} = 0.35$, $M_{max} = 1.4$, and the voltage range $R = 4$.

V. Experimental Results

In order to verify the feasibility of the proposed converter and control strategy, an 800-W prototype with 100–400-V input voltage and 380-V output voltage is built. Turns ratio of transformer is 14:38, $R = 4$, and M is 0.35–1.4, the system parameters are listed in Table II.

Fig. 20 shows the control block diagram of the hybrid three-level full-bridge IBB converter under optimal control

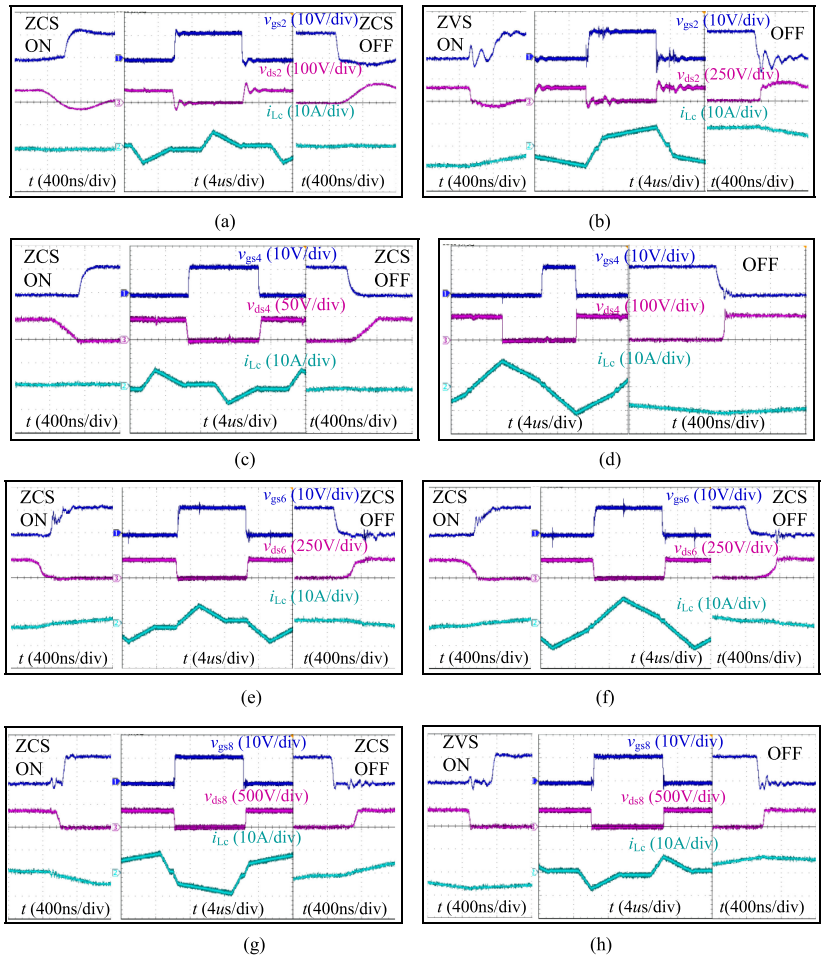

Fig. 22. Switching waveforms of Q_2, Q_4, Q_6, and Q_8 at different operational areas. (a) Q_2 $V_{\text{in}} = 100$ V, $P_{\text{o}} = 200$ W. (b) Q_2 $V_{\text{in}} = 300$ V, $P_{\text{o}} = 800$ W. (c) Q_4 $V_{\text{in}} = 100$ V, $P_{\text{o}} = 200$ W. (d) Q_4 $V_{\text{in}} = 200$ V, $P_{\text{o}} = 800$ W. (e) Q_6 $V_{\text{in}} = 200$ V, $P_{\text{o}} = 400$ W. (f) Q_6 $V_{\text{in}} = 200$ V, $P_{\text{o}} = 800$ W. (g) Q_8 $V_{\text{in}} = 300$ V, $P_{\text{o}} = 800$ W. (h) Q_8 $V_{\text{in}} = 100$ V, $P_{\text{o}} = 200$ W.

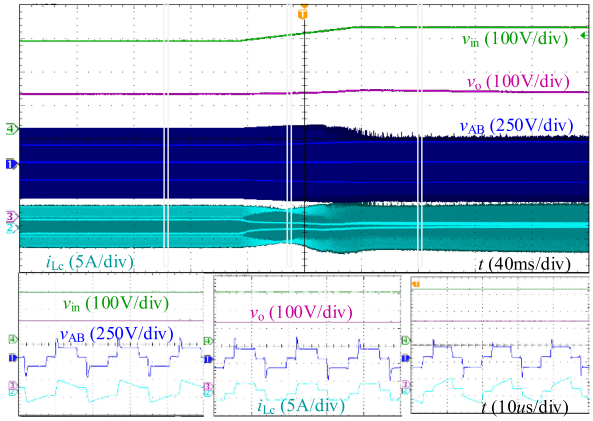

Fig. 23. Experimental waveforms of modes transition in the case of input voltage step.

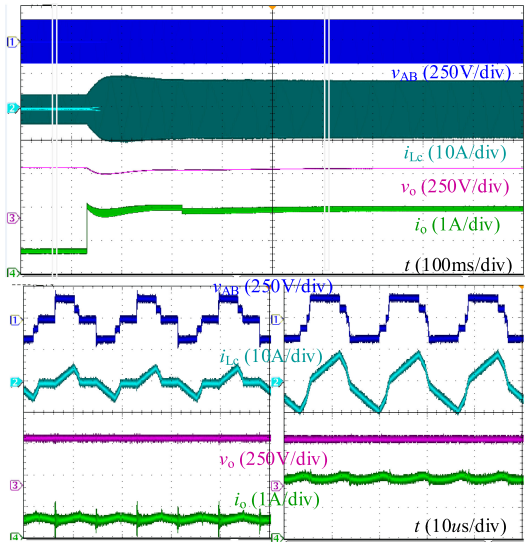

Fig. 24. Experimental waveforms of modes transition in the case of load step.

trajectory with three control variables, which is similar to the control block diagram in [20]. The output voltage is sampled, and then compared with the reference voltage to get the error signal v_{e}, and calculated with the sampled input voltage to get the value of M. v_{e} is sent to PI controller to generate the control signal v_{c}. Optimal control strategies block generate the control variables D_1, D_2, and D_3. After gate signal generation block, duty ratios are transferred to the gate signals of switches. The

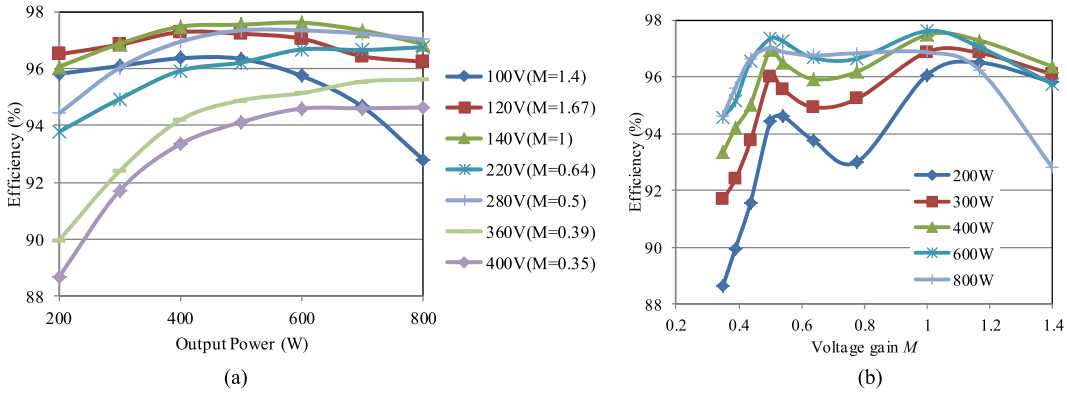

Fig. 25. Efficiency curves. (a) Efficiency curves versus output power at different input voltages. (b) Efficiency curves versus voltage gain at different output powers.

control strategy can be implemented by digital signal processor TMS320F28035 easily.

Fig. 21 shows the experimental waveforms of a hybrid three-level full-bridge IBB converter. When $M = 1$, $V_{\text{in}} = 140$ V, and when $M = 0.5$, $V_{\text{in}} = 280$ V. Fig. 21(a), (c), and (f) shows waveforms in DCM mode corresponding to $M > 1$, $0.5 < M < 1$, $M < 0.5$, respectively. Fig. 21(b), (d), and (e) shows waveforms in BCM mode corresponding to $M > 1$, $0.5 < M < 1$, $M < 0.5$ respectively. Fig. 21(f) shows that v_{AB} appears $\pm V_{\text{in}}$ spikes in the initial of each half cycle in DCM when $M < 0.5$. During this stage, the junction capacitor of Q_1 or Q_4 is charged by the clamp inductor current, which cannot be avoided.

Fig. 22 shows the voltage waveforms of v_{gs} and v_{ds} of primary-side and secondary-side switches in different operational areas. ZCS or ZVS of both primary-side and secondary-side switches can be achieved. Due to the influence of the junction capacitors of power devices and clamped inductors, there may be resonance at the process of Q_2 ON and OFF.

The waveform of modes transition in the case of input-voltage step is shown in Fig. 23. When the load power is 200 W, the input-voltage steps up from 260 to 300 V that crossing the point of $M = 0.5$. The peak current of the clamped inductor decreases first and then increases, which is in accordance with the theoretical analysis. The waveforms of three different input voltages are shown. As the relationship between the input voltage and output voltage changes, the slope of an inductor current varies accordingly in the direct energy transfer stage (D_2).

The waveform of modes transition in the case of load step is shown in Fig. 24. The input voltage is constant 160 V, and the load power is changed from 200 to 700 W. When the load step occurs, the converter's operational mode switches from DCM to BCM.

The efficiency curves are shown in Fig. 25. Fig. 25(a) shows the efficiency versus output power under the input voltages 100, 120, 140, 220, 280, 360, and 400 V. The values of voltage gain M corresponding are given. The maximum efficiency is 97.61% when input voltage is 140 V ($M = 1$) and output power is 600 W. When the input voltage is 280 V ($M = 0.5$), the peak efficiency is 97.34% with the output power is 500 or 600 W. The peak efficiency of $M = 1$ is better than that of $M = 0.5$ for the existence of the $\pm V_{\text{in}}$ voltage spikes of v_{AB}. When the input voltage is 100 V, the efficiency decreases at heavy load because the conduction loss increasing significantly. When the input voltage is 360 or 400 V, the efficiency is the lowest at light load. At this time, the switching losses of Q_5 and Q_6 are playing a dominant role in the whole converter efficiency. Fig. 25(b) shows the efficiency versus voltage gain M under output powers 200, 300, 400, 600, and 800 W. There are two maximum efficiency points, which appear at $M = 0.5$ and $M = 1$. If $M > 1.2$ or $M < 0.4$, the efficiency decreases obviously, which is because the peak current of the clamped inductor is increasing.

In Fig. 25, most of the operating points are higher than 94%. The experimental results indicate that the hybrid three-level full-bridge IBB converter with clamped inductor can achieve smooth mode transition, can operate at wider voltage range as $R = 4$, and can be regulated at full load range with high efficiency.

VI. Conclusion

A hybrid three-level full-bridge IBB converter with clamped inductor and its control strategy is proposed in this paper. With the simplification of control variables in BCM or DCM, the operational modes are reduced, and smooth mode transition is possible. Key features of the proposed converter and control strategy are as follows.

1) The proposed converter's five variable voltage levels in primary-side port, i.e., $\pm V_{\text{in}}$, $\pm V_{\text{in}}/2$, and zero level, leading to a wider voltage range than normal IBB converters.
2) Low-voltage stress of Q_1, Q_2, Q_3, and Q_4 which is half of the V_{in}.
3) Wide voltage range regulation through simple fixed-frequency phase-shift control, and smoothly mode transition. Compared with conventional DAB or semi-DAB converters, the voltage range is doubled.
4) Low circulating energy because the converter always operates in BCM or DCM.
5) ZVS and ZCS of all the devices in primary-side circuit and secondary-side circuit regardless of input voltage or output power.

6) Low-current peak value and low-current stress of power devices compared with semi-DAB converter.
7) There are eight switches and four diodes, thus the complexity of the converter is increased. The number of operational modes increases and the control strategy is complex.

All these key features combine to result in a high-efficiency IBB converter that is ideal for wider voltage range applications. The key features were verified using an 800-W prototype. The control strategy with three control variables can be applied to other IBB converter derivations.

REFERENCES

[1] F. Krismer and J. W. Kolar, "Efficiency-optimized high-current dual active bridge converter for automotive applications," *IEEE Trans. Ind. Electron.*, vol. 59, no. 7, pp. 2745–2760, Jul. 2012.

[2] F. Liu and X. Ruan, "ZVS combined three-level converter—A topology suitable for high input voltage with wide range applications," *IEEE Trans. Ind. Electron.*, vol. 54, no. 2, pp. 1061–1072, Apr. 2007.

[3] H. Wu, Y. Li, and Y. Xing, "LLC resonant converter with semiactive variable-structure rectifier (SA-VSR) for wide output voltage range application," *IEEE Trans. Power Electron.*, vol. 31, no. 5, pp. 3389–3394, May 2016.

[4] C. Yao, X. Ruan, and X. Wang, "Automatic mode-shifting control strategy with input voltage feed-forward for full-bridge-boost DC–DC converter suitable for wide input voltage range," *IEEE Trans. Power Electron.*, vol. 30, no. 3, pp. 1668–1682, Mar. 2015.

[5] W. Li, S. Zong, F. Liu, H. Yang, X. He, and B. Wu, "Secondary-side phase-shift-controlled ZVS DC/DC converter with wide voltage gain for high input voltage applications," *IEEE Trans. Power Electron.*, vol. 28, no. 11, pp. 5128–5139, Nov. 2013.

[6] C. Yao, X. Ruan, X. Wang, and C. K. Tse, "Isolated buck–boost DC/DC converters suitable for wide input-voltage range," *IEEE Trans. Power Electron.*, vol. 26, no. 9, pp. 2599–2613, Sep. 2011.

[7] R. Beiranvand, B. Rashidian, M. R. Zolghadri, and S. M. H. Alavi, "Using LLC resonant converter for designing wide-range voltage source," *IEEE Trans. Ind. Electron.*, vol. 58, no. 5, pp. 1746–1756, May 2011.

[8] X. Zhao, L. Zhang, R. Born, and J.-S. Lai, "A high-efficiency hybrid resonant converter with wide-input regulation for photovoltaic applications," *IEEE Trans. Ind. Electron.*, vol. 65, no. 5, pp. 3684–3695, May 2017.

[9] T. LaBella, W. Yu, J. S. Lai, M. Senesky, and D. Anderson, "A bidirectional-switch-based wide-input range high-efficiency isolated resonant converter for photovoltaic applications," *IEEE Trans. Power Electron.*, vol. 29, no. 7, pp. 3473–3484, Jul. 2014.

[10] X. Sun, X. Li, Y. Shen, B. Wang, and X. Guo, "Dual-bridge LLC resonant converter with fixed-frequency PWM control for wide input applications," *IEEE Trans. Power Electron.*, vol. 32, no. 1, pp. 69–80, Jan. 2017

[11] H. Wu, L. Chen, and Y. Xing, "Secondary-side phase-shift-controlled dual-transformer-based asymmetrical dual-bridge converter with wide voltage gain," *IEEE Trans. Power Electron.*, vol. 30, no. 10, pp. 5381–5392, Oct. 2015.

[12] W. Sun, H. Wu, H. Hu, and Y. Xing, "Modified LLC resonant converter with secondary paralleled bidirectional switch for applications with hold-up time requirement," *IET Power Electron.*, vol. 10, no. 3, pp. 398–404, Mar. 2017.

[13] H. Li, Z. Li, L. Zhao, and J. Zhang, "Multi-level control strategy of wide input LLC resonant converter," in *Trans. China Electron. Soc.*, vol. 32, no. 4, pp. 48–57, Feb. 2017.

[14] K. Jin and X. Ruan, "Hybrid full-bridge three-level LLC resonant converter—A novel DC-DC converter suitable for fuel-cell power system," *IEEE Trans. Ind. Electron.*, vol. 53, no. 5, pp. 1492–1503, Oct. 2006.

[15] Y. Lu, H. Wu, K. Sun, and Y. Xing, "A Family of isolated buck-boost converters based on semiactive rectifiers for high-output voltage applications," *IEEE Trans. Power Electron.*, vol. 31, no. 9, pp. 6327–6340, Sep. 2016.

[16] H. Wu, T. Mu, H. Ge, and Y. Xing, "Full-range soft-switching-isolated buck-boost converters with integrated interleaved boost converter and phase-shifted control," *IEEE Trans. Power Electron.*, vol. 31, no. 2, pp. 987–999, Feb. 2016.

[17] H. Wu, Y. Lu, K. Sun, and Y. Xing, "Phase-shift-controlled isolated buck-boost converter with active-clamped three-level rectifier (AC-TLR) featuring soft-switching within wide operation range," *IEEE Trans. Power Electron.*, vol. 31, no. 3, pp. 2372–2386, Mar. 2016.

[18] H. Wu, Y. Lu, T. Mu, and Y. Xing, "A family of soft-switching DC–DC converters based on a phase-shift-controlled active boost rectifier," *IEEE Trans. Power Electron.*, vol. 30, no. 2, pp. 657–667, Feb. 2015.

[19] B. Zhao, Q. Song, W. Liu, and Y. Sun, "Overview of dual-active-bridge isolated bidirectional DC–DC converter for high-frequency-link power-conversion system," *IEEE Trans. Power Electron.*, vol. 29, no. 8, pp. 4091–4106, Aug. 2014.

[20] H. Zhou and A. M. Khambadkone, "Hybrid modulation for dual-active-bridge bidirectional converter with extended power range for ultracapacitor application," *IEEE Trans. Ind. Appl.*, vol. 45, no. 4, pp. 1434–1442, Jul./Aug. 2009.

[21] F. Li, Y. Li, and X. You, "Optimal dual-phase-shift control strategy of isolated buck-boost converter with clamped inductor," *IEEE Trans. Power Electron.*, vol. 33, no. 6, pp. 5374–5385, Jun. 2018.

Yan Li (M'08) was born in Heilongjiang Province, China, in 1977. She received the B.S. and M.S. degrees in electrical engineering from Yanshan University, Qinhuangdao, China, in 1999 and 2003, respectively, and the Ph.D. degree in electrical engineering from Nanjing University of Aeronautics and Astronautics, Nanjing, China, in 2009.

From 1999 to 2009, she was with Yanshan University. She was a Visiting Scholar with the Bradley Department of Electrical and Computer Engineering, Virginia Tech. Since 2009, she has been with the Faculty of Electrical Engineering, Beijing Jiaotong University, Beijing, China, where she is currently an Associated Professor with the College of Electrical Engineering. Her current research interests include multiple-input dc/dc converters, renewable power systems, PV grid-tied system, and application of widebandgap power semiconductor devices.

Fang Li was born in Hebei Province, China, in 1988. She received the B.S. degree in electrical engineering from China University of Petroleum, Dongying, China, in 2010, and the M.S. degree and the Ph.D. degree in electrical engineering from Beijing Jiaotong University, Beijing, China, in 2012 and 2017, respectively.

She is currently a Postdoctoral Researcher in power electronics with Beijing Jiaotong University. Her research interests include spacecraft power systems and high-frequency soft-switching dc/dc converters.

Fang-Wei Zhao (S'17) was born in Xinzhou, Shanxi Province, China, in 1995. She received the B.S. degree in electrical engineering from Beijing Jiaotong University, Beijing, China, in 2013, where she is currently working toward the Ph.D. degree.

Her current research interests include multiple-input dc/dc converters and application of widebandgap power semiconductor devices.

Xiao-Jie You was born in Fujian Province, China, in 1964. He received the M.S. degree in electrical engineering from China Agricultural University, Beijing, China, in 1989, and the Ph.D. degree in electrical engineering from Czech Technical University, Prague, Czech Republic, in 2001.

He is currently a Professor and Director with the Power Electronic Research Institute, School of Electrical Engineering, Beijing Jiaotong University, Beijing. His current research interests include ac drive electric locomotive control, switching power control, active power filters, and power quality control.

Kun Zhang was born in Shanxi Province, China, in 1992. He received the B.Sc. degree in electronic engineering from Beijing Jiaotong University, Beijing, China, in 2018.

Since 2018, he has been with Beijing Satellite Manufacturing Plant Co., Ltd., Beijing. His current research focuses on dc/dc converters.

Mei Liang (M'13) was born in Hebei Province, China, in 1988. She received the B.Sc. and Ph.D. degrees in electronic engineering from Beijing Jiaotong University, Beijing, China, in 2011 and 2018, respectively.

Since 2018, she has been with Cooperate Research Center, ABB China, Ltd., Beijing, as a Scientist. Her research interests include analysis of power electronics converter topologies, efficient switching techniques, and widebandgap semiconductor applied research.